Micron 190 (2025) 103746

Contents lists available at ScienceDirect

Micron

journal homepage: www.elsevier.com/locate/micron

Visualizing the Li distribution in an all-solid-state battery composite electrode using combined plasma focused-ion beam microscopy and secondary-ion mass spectroscopy

Yige Sun [a,b,*], Gareth M. Hughes [a], Junfu Bu [a,b], Junliang Liu [a], Chris R.M. Grovenor [a], Patrick S. Grant [a,b]

[a] Department of Materials, University of Oxford, Parks Road, Oxford OX1 3PH, United Kingdom
[b] The Faraday Institution, Quad One, Harwell Science and Innovation Campus, Didcot OX11 ORA, United Kingdom

ARTICLE INFO

Keywords:
Plasma FIB
SIMS
Battery
Lithium distribution
Correlative mapping

ABSTRACT

Using a Li metal anode, the all-solid-state battery (ASSB) promises a step change in specific energy over Li-ion batteries and the potential for increased battery safety. ASSBs rely critically on the efficient movement of Li charge carriers through a Li-conducting solid electrolyte (SE) separator and throughout a composite cathode (CC) comprising active particles, particulate SE, polymeric binder, and carbon. Unfortunately, there is no readily accessible laboratory method to visualise Li distributions at both particle and electrode scales to help understand and optimise Li electrode dynamics in ASSBs. We report a method to map all electrode elements in a 3D volume, including Li, within a typical ASSB composite cathode. The method combines a xenon plasma focused-ion beam (PFIB) for 3D milling, energy dispersive X-ray spectroscopy (EDS) to map non-Li elements, and secondary ion mass spectrometry (SIMS) to map Li. We manipulate 3D EDS and SIMS datasets into a common format and then recombine them in 3D to differentiate the different materials at high resolution. This new approach can be applied to understand and optimise the role of microstructure in controlling ASSB performance.

1. Introduction

Although the lithium-ion battery (LIB) is playing an important role in securing the transition to a low-carbon economy, significant improvements in battery specific energy can be achieved if the liquid electrolyte in a LIB is replaced by a solid electrolyte (SE) that is sufficiently inert that a high-capacity Li metallic anode can replace conventionally used graphite (Randau et al., 2020; Yim et al., 2023; Pasta et al., 2020). SEs are also generally non-flammable so that the resulting all-solid-state battery (ASSB) has a lower susceptibility to fire compared with LIBs.

The typical configuration of an ASSB involves the integration of a SE separator, generally a ceramic (*e.g.* $Li_7La_3Zr_2O_{12}$ (LLZO)) between an anode (*e.g.* Li metal) and a composite cathode (*e.g.* $LiCoO_2$ + SE + polymeric binder + carbon). During ASSB charging, Li^+ ions move from the cathode, through the SE separator, to the anodic current collector to plate, ideally, a homogeneous layer of pure Li, sometimes with the help of an interlayer, while avoiding heterogeneous plating and growth of Li dendrites back to the cathode and a short-circuit (Dominic Spencer-Jolly et al., 2023; Ning et al., 2023). To understand and optimize ASSB performance during charge and discharge, and degradation in service under a range of conditions, visualization of the Li distribution across the electrochemical cell at the micro-meter scale is therefore highly desirable since the overall Li spatial distribution across the cell and in the active particles of the composite cathode determines the overall state of charge of the ASSB.

So far, insights into the effect of the spatial and temporal distribution of Li on ASSB performance has predominantly been provided by modelling of electrode dynamics, or experimentally by various indirect methods based on electrochemical testing. Therefore there remains an opportunity to develop a relatively easy-to-access laboratory technique that can map Li distributions with useful sensitivity, resolution and over the length scale of interest to the operation of an ASSB (Bucci et al., 2017; Nomura et al., 2020a, 2020b). However, there are significant challenges in the visualisation of Li in ASSB electrodes relating to having a technique with sufficient Li detection sensitivity at sufficiently fine-scale resolution (< 1μm), and which can also then map the spatial distribution of Li at this resolution over larger length scales. It would also be desirable to visualise the Li distributioin in 3D, and to be able to

* Corresponding author at: Department of Materials, University of Oxford, Parks Road, Oxford OX1 3PH, United Kingdom.
E-mail address: yige.sun@materials.ox.ac.uk (Y. Sun).

https://doi.org/10.1016/j.micron.2024.103746
Received 23 April 2024; Received in revised form 19 October 2024; Accepted 12 November 2024
Available online 24 November 2024

map other elements (by the same or a different technique) simultaneously, and to correlate these elemental maps with the Li distribution.

Energy dispersive X-ray Spectroscopy (EDS) is a common and mature technique for elemental analysis in a scanning electron microscope (SEM) and is used widely for studying elemental distributions across electrode cross-sections, with micron or better resolution. However, Li detection is difficult using EDS due to (i) the relatively low X-ray energy of Li, (ii) the low probability of X-ray emission under electron irradiation, and (iii) the high likelihood of Li X-ray absorption (Hovington et al., 2016; Osterreicher et al., 2021). Other microscopy-based techniques that are commonly used to map elemental distributions include Raman imaging, X-ray photoelectron spectroscopy (XPS), and X-ray absorption near-edge structure (XANES) spectroscopy (Otoyama et al., 2016; Wood et al., 2018; Pattammattel et al., 2020). However, the combination of either limited sensitivity and/or spatial resolution, make them unsuitable or at best difficult to use for mapping elemental Li in battery electrodes.

At higher resolution, approximately atomic scale element mapping can be achieved using atom probe tomography, high-angle annular dark-field scanning transmission electron microscopy (HAADF-STEM), or STEM-electron energy loss spectroscopy (STEM-EELS) (Kim et al., 2022; Gong et al., 2018; Nomura et al., 2018). Nonetheless, sample preparation for STEM and the other analyses presents challenges when dealing with Li-containing samples due to ion-beam damage (Koh et al., 2023). These methods also have limited field-of-view, typically below 100 nm x100 nm, and therefore cannot readily be used for mapping Li distributions at the electrode scale, required to rationalise overall SSB energy storage behaviour. Spatially resolved nuclear magnetic resonance (NMR) spectroscopy is used for *in situ* and operando investigations of lithium-ion batteries (Trease et al., 2012; Marker et al., 2020). However, relatively large special cells are required and there are challenges in data interpretation (Torres and Price, 2016; Fang et al., 2022).

Indirect methods for obtaining local Li concentrations include spatially resolved X-ray or neutron diffraction where shifts in lattice spacings of well-characterised crystalline and electrochemically active phases can be correlated with local Li concentration (Robinson et al., 2019; Manawan et al., 2021; Ziesche et al., 2020). While these diffraction approaches have the substantial advantage that they can be used in operando, they require specialist electrochemical cells, for example with unrealistically thick (millimeter-scale) electrodes. Further, the required high spatial resolution X-ray and neutron sources can generally only be accessed at major national facilities.

Secondary-ion mass spectrometry (SIMS) can resolve light elements such as Li in electrode cross-sections. In SIMS, a charged primary ion beam is focused and used to bombard a sample surface. The ion bombardment results in sputtering or removal of the top few atomic layers of material. Secondary ions are then generated, which can be manipulated by a magnetic field into a mass spectrometer, which analyses the ions or charged molecular fragments according to their mass-to-charge ratio. Based on the total primary ion dose, there are two SIMS modes: static and dynamic, where the static limit is defined as 10^{13} ion/cm^2 (Guilhaus, 2005).

Below this limit, static SIMS (*e.g.* with a time-of-flight mass spectrometer, ToF-SIMS) uses a relatively low dose such that each primary ion interacts with the surface that has not been damaged by a previous primary ion. Therefore, typically less than 1 % of the surface constituents receive primary ion impacts. Static SIMS has been broadly applied to study Li in LIB. The type of information regarding Li distribution by static SIMS includes electrode surface characterization and active material/electrolyte interfacial degradation at around 0.1–1 μm depth (Lindon et al., 2016; Yamagishi et al., 2020; Ohnishi et al., 2012).

Dynamic SIMS (*e.g.* with a quadrupole detector) uses a higher dose of approximately 10^{17} ions/cm^2, which results in a continuous etching of the surface (Mei et al., 2022). Compared with TOF-SIMS, dynamic SIMS exhibits a lower mass resolution, but has better sensitivity (10^{13} atoms/cm^3), a larger analysed area (2 ×2 up to 250 ×250 μm^2), and a wider dynamic detection range (5 ×10^{12} to 5 ×10^{22} atoms/cm^3) (Lindon et al., 2016; Mei et al., 2022). Dynamic SIMS can be used to obtain elemental information below the initial surface, *e.g.* chemical information as a function of depth (depth profile) for example to study elemental distributions in semiconductor and solar cell devices (Brown et al., 1986; Treat et al., 2011). Recently, dynamic SIMS has been applied to ASSBs to determine Li diffusivity in a $Li_7La_3Zr_2O_{12}$ (LLZO) electrolyte and in $LiMn_2O_4$ thin films, as well as to study the impact of water on the cathode, anode, and separator in LIBs (Brugge et al., 2021; Kuwata et al., 2018; Wilhelm et al., 2024).

These studies typically use either Ga^+, Cs^+ or 0^- primary ions, which can result in beam-induced damage and selective enhancement of the ionization probability (Cs^+ bombardment results in high negative ion generation, and 0^- bombardment high positive ion generation) (Burnett et al., 2016; Pillatsch et al., 2019). The intensity of the detected SIMS signal for any particular species is not solely influenced by the local concentration but also by other factors such as the overall local chemistry and crystallography of the material (known as matrix effects), surface topography, charging effects, *etc.* These factors collectively contribute to variations in the sputter yield, which can span several orders of magnitude, and makes the quantification of SIMS data for element concentrations difficult (Werner, 1980; Moore et al., 2012; Laegreid and Wehner, 1961).

In this paper, we introduce a novel approach for mapping the spatial distribution of Li and non-Li elements in an ASSB composite electrode at the micrometer scale. Expanding upon previous work that utilized automated three-dimensional EDS analysis with a dual-beam FIB only, we now combine a Xe^+ plasma-focused ion beam (PFIB), EDS and dynamic SIMS (Schaffer et al., 2007). The integration of EDS and SIMS provides complementary analytical capabilities, offering an overall more comprehensive and detailed characterization of the material. We describe how EDS and SIMS maps were obtained from the same electrode cross-section, and how the different elemental maps were then combined and cross-correlated, even though they were obtained over only partially overlapping areas and at different spatial resolutions. We show the utility of a Xe^+ plasma for removing controlled thicknesses of relatively large area layers of an electrode, and how the EDS-SIMS correlation methodology can be applied for each newly revealed surface so that 3D elemental maps, including for Li, were obtained. The methodology provides a tool to probe the behaviour of Li-based electrochemical energy storage devices and may help the development of improved active materials and the design of more efficient electrode microstructures.

2. Materials and methods

2.1. Electrode preparation

A composite cathode for an all-solid-state battery (ASSB) was used to develop the PFIB SIMS methodology, which has been described elsewhere (Kim and Rupp, 2020; Ren et al., 2023). Briefly, the cathode compromised Al_20_3-coated-$LiCo0_2$ (LCO) as the active material, $Li_{6.4}La_3Zr_{1.4}Ta_{0.6}0_{12}$ (LLZTO, cubic phase) powder as the solid electrolyte (SE) and Super P (SP) fine-scale carbon powder as the conductivity enhancer. The LCO was intended to be coated by Al_20_3 to improve interfacial stability in contact with LLZO by mixing aluminium isopropoxide and LCO powder in isopropyl alcohol (IPA) and stirring for 2 hours (Gurung et al., 2019). The suspension was dried in a vacuum oven at 120℃ overnight to obtain LCO coated with 1 *wt*% Al_20_3. Then, 47.5 *wt*% LLZTO, 47.5 *wt*% Al_20_3 coated LCO and 5 *wt*% SP were ball milled with IPA for 1 hr. The mixture was dried in a vacuum oven at 120℃ overnight. Finally, 2 g of the dry LLZTO/Al_20_3-coated-LCO/SP mixture was loaded into a graphite mould and sintered in a Field Assisted Sintering Technology (FAST) machine at 600℃ for 5 min and 50 MPa, to form a dense 16 mm diameter and 1.5 mm thick pellet (Bu et al., 2016).

2.2. Instrumentation

2.2.1. Plasma FIB

The electrode was judged air and moisture sensitive, and therefore a vacuum transfer facility (Gatan iLoad, Pleasanton USA) was used to transfer electrodes from the glovebox to the PFIB chamber under an inert atmosphere.

FIB serial sectioning is employed widely to reconstruct 3D volumes from a series of 2D images/maps. The majority of FIB systems use a Ga^+ liquid metal ion source (LMIS) as the ion beam, principally for milling (although it can also be utilised for some imaging modes). Ga^+ LMIS FIB systems are capable of high voxel resolution (10 ~ 600 nm voxel size) but are generally restricted to a relatively small total volume of up to $30 \times 30 \times 30$ μm^3, limited by extended milling times, poor surface finishes due to high current used for sectioning, a spot size of $d_{50} \sim 2$ µm and various geometrical constraints relating to the layout of the sample chamber (Burnett et al., 2016; Cantoni and Holzer, 2014).

In contrast, PFIB uses a Xe^+ inductively coupled plasma (ICP) source resulting in a superior angular intensity and a smaller spot size ($d_{50} \sim$ 800 nm) at a high current *e.g.* 100 nA *(c.f.* over 1 µm for Ga^+ FIB) (Burnett et al., 2016). Currents in the µA range are also possible with an ICP source. Thus PFIB exhibits a faster sputter rate (0.41 μm^3/nC for Xe^+ compared with 0.31μm^3/nC for Ga^+ in sectioning Al) (Burnett et al., 2016). Nevertheless, a Xe^+ PFIB creates 20–40 % less beam damage and avoid the formation of Ga residue (Burnett et al., 2016; Ko et al., 2007). As Xe^+ processes through the target, it loses energy relatively quickly with a depth of ion penetration of ~25 nm compared with ~38 nm for Ga^+ (Burnett et al., 2016; Liu et al., 2020). PFIB allows milling of greater areas and volumes ($> 200 \times 100 \times 200$ μm^3) which is well-matched to the dimensions of an ASSB and related electrodes.

A Thermo Scientific™ Helios™ G4 PFIB CXe DualBeam™ Plasma FIB/SEM fitted with an Oxford Instruments Ultim Max 170 Energy Dispersive X-ray detector (EDS) and a Hiden EQS SIMS were used for cross-sectioning, imaging, EDS and SIMS element mapping respectively. The Hiden EQS SIMS is a quadrupole SIMS that consists of four parallel metal rods with applied RF and DC voltages, causing ions to oscillate based on their mass-to-charge (m/q) ratio (Pillatsch et al., 2019). Only ions within a specific m/q range resonate with the electrical field and reach the detector, while others are discarded. This arrangement allows for the detection of one mass at a time, and rapid switching of quadrupole parameters enables detection of multiple masses, with imaging data potentially coming from different sample locations. The system has a compact and lightweight design that makes it suitable for coupling with PFIB instruments.

A schematic of the PFIB chamber is shown in Fig. 1, indicating primary columns (SEM and PFIB), detectors (SIMS and EDS), and the different sample orientations. The angle between the SEM column and the PFIB column was 52°. Between the PFIB column and the SIMS detector, the angle was 56°. The working distance of the electron beam was 4 mm and 16.5 mm for the Xe^+ ion beam. In order to exploit a slice and view workflow with SIMS analysis on the cross-sectional face, it was necessary to design and apply a pre-tilt geometry via a custom holder.

Since the settings of the primary ion beam in SIMS are known to influence the ionisation probability and yields of the electrode elements (Whitlow et al., 1987; Stevie et al., 2014), we first investigated the effects of beam current on signal yield and the sputter rate on a single crystal <110> Si wafer. Supporting Information Table S1 and Fig. S1 show the depth of penetration in each SIMS scan of the Xe^+ ion into a reference Si wafer at increasing primary ion beam currents. The higher the beam current, the higher the ion dose density applied per point/dwell point at the same dwell time, and the larger the sputter rates. Based on these parametric explorations, and taking care not to saturate the detector, we chose Xe^+ ion beam conditions of 30 keV and 1 nA to map the $^6Li^+$ isotopic signal for SIMS analysis. In this experiment a 500 × 500 pixel map was acquired and each map took approximately 5 min to acquire.

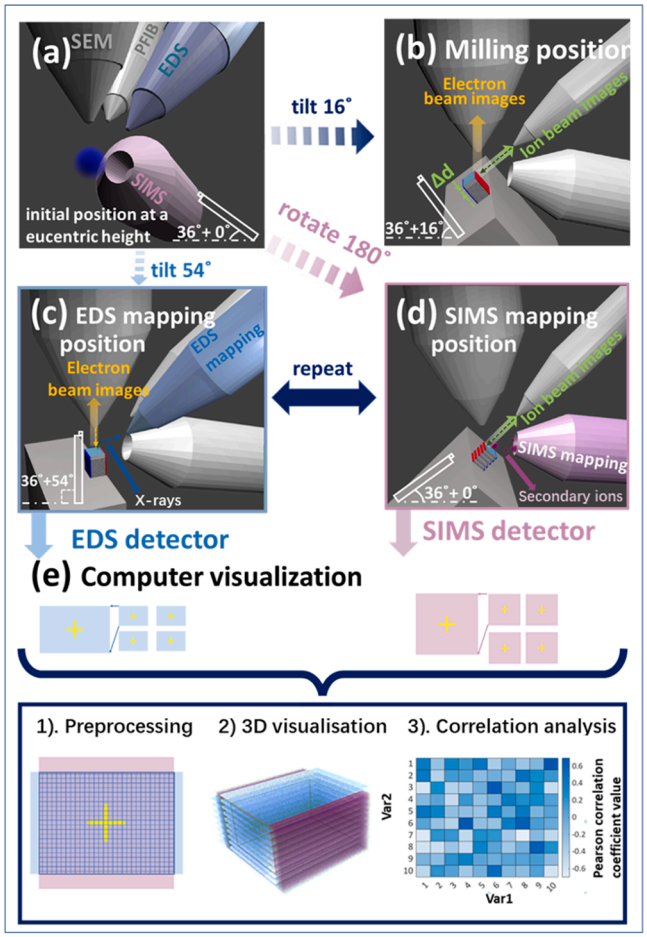

Fig. 1. Workflow of data capture and 3D reconstruction. (a) The relative position of the PFIB column, SEM column, EDS detector, and SIMS detector at position 1. Holder pre-tilted to 36°. (b) Holder tilted 16° from the initial position to the milling position 2 with the sample cross-section surface facing the ion beam column. (c) Holder tilted 54° from the initial position to EDS mapping position 3 with the sample cross-section surface facing the electron beam column. (d) Holder rotated 180° from the initial position to SIMS mapping position 4 with the cross-section surface facing the ion beam column. (e) EDS and SIMS maps recorded from partially overlapping areas of interest.

2.2.2. Workflow for milling, imaging, EDS and SIMS elemental mapping

In order to be able to polish and mill the electrode cross-section, apply secondary and backscatter electron imaging, and obtain EDS and SIMS elemental maps, a new workflow was established. The region of interest of the bulk cathode was first identified and then isolated using a lift-out method to attach the volume to a Si wafer (Robertson et al., 2020).

The workflow then involved the following steps:

1) Locate the sample at the eucentric height and tilt of 36° to the horizontal (position 1, Fig. 1(a)).
2) Polish the electrode cross-section surface at a tilt angle of 16° (position 2, Fig. 1(b)). The Xe^+ ion beam (dark green dotted line) was horizontal to the cross-section (light blue).
3) Obtain SEM images (secondary electron, SE, and backscattered electron, BSE) and EDS elemental map at a tilt angle of 54° (position 3, Fig. 1(c)). The cross-section surface is normal to the SEM column and electron beam (orange dotted line). EDS element maps were obtained typically for Co Lα1,2, C Kα1_2, Zr Lα1 and Al Kα1 at 5 KeV and 1.6 nA, with each map taking approximately 5 min to acquire. The accelerating voltage was chosen initially to excite the K-lines for EDS analyses, to avoid overlaps if using lower energy L- and M-

peaks. In our previous work, we used a 10 nA electron beam for electron backscatter diffraction (EBSD) scans on LIB cathodes with no significant damage (Doerrer et al., 2021). In this study, a beam current of 1.6 nA was used and provided sufficient count rate at a short dwell time, which may also help to reduce migration of Li due to beam heating.

4) Obtain ion beam images and SIMS maps at a rotation angle of 180° (position 4, Fig. 1(d)). The finely polished electrode cross-section faced the ion beam. The Xe^+ ion beam scanned and bombarded the surface to induce a fragmentation cascade.
5) Repeat steps 3 and 4 n times (typically $n = 39$, which took approximately 12 hr, including both data acquisition and precise cross-sectioning) to build up a 3D data set.
6) Tilt back to position 2 to estimate the total milled depth from ion beam images.

2.3. Data processing

Having acquired SEM images, and EDS and SIMS maps, algorithms and image manipulation protocols were required to allow merging and correlation of SIMS and EDS data because they were obtained at different resolutions, with different count intensities, and from only partially overlapping areas *e.g.* SIMS maps were square and EDS maps were rectangular (Fig. 1(e)).

First, the EDS maps were analysed using Aztec software (Oxford Instruments, AZtec 4.1 SP1). Maps were 17.6 × 28.7 μm^2 (216 × 352 pixels, binning factor 4 to match SIMS pixel size, and to improve signal/noise of short EDS scans dwell time) with a resultant pixel size of 81.4 nm. Then the SIMS maps were analysed using MAPPER software (Hiden, Warrington UK) and were 36 × 36 μm^2 (500 × 500 pixels). The approximate SIMS pixel size was estimated as 72 nm.

MATLAB was then used to express each 2D element or chemical species (EDS and SIMS) map in each slice as a 3D data matrix, where x and y referred to the spatial position of the measurement and z was signal count (intensity). In each slice, the digital images were composed of two-dimensional arrays of integers representing individual picture elements, or pixels. The number of bits used to represent each pixel described the number of possible gray levels. If n bits are used, there are 2^n possible pixel values, ranging from 0 (black) to ($2^n - 1$) (white), with intermediate values representing shades of gray there. For 8-bit images, the pixel values range from 0 to 255. An image histogram plotted (intensity frequency plots) pixel intensity (x-axis) versus the number of pixels (y-axis), showing all possible gray levels (0–255 for an 8-bit image) and the frequency of each intensity across the image.

Since EDS and SIMS raw data often show significant disparities in intensity scales due to the different physical mechanisms involved, the data sets were normalized. To assess the impact of this normalization, Fig. 2(a1) and 2(a2) show typical intensity frequency plots as a function of the pixel intensity interval respectively. Two different approaches for the normalisation of the EDS and SIMS data were explored.

i. Min-max scaling normalization:

$$x^* = \frac{x - x_{\min}}{x_{\max} - x_{\min}} \tag{1}$$

ii. Logarithm transformation normalization: (Metcalf and Casey, 2016)

$$x^* = \frac{\log_{10} x}{\log_{10} x_{\max}} \tag{2}$$

where x is the original intensity value, x^* is the normalized intensity

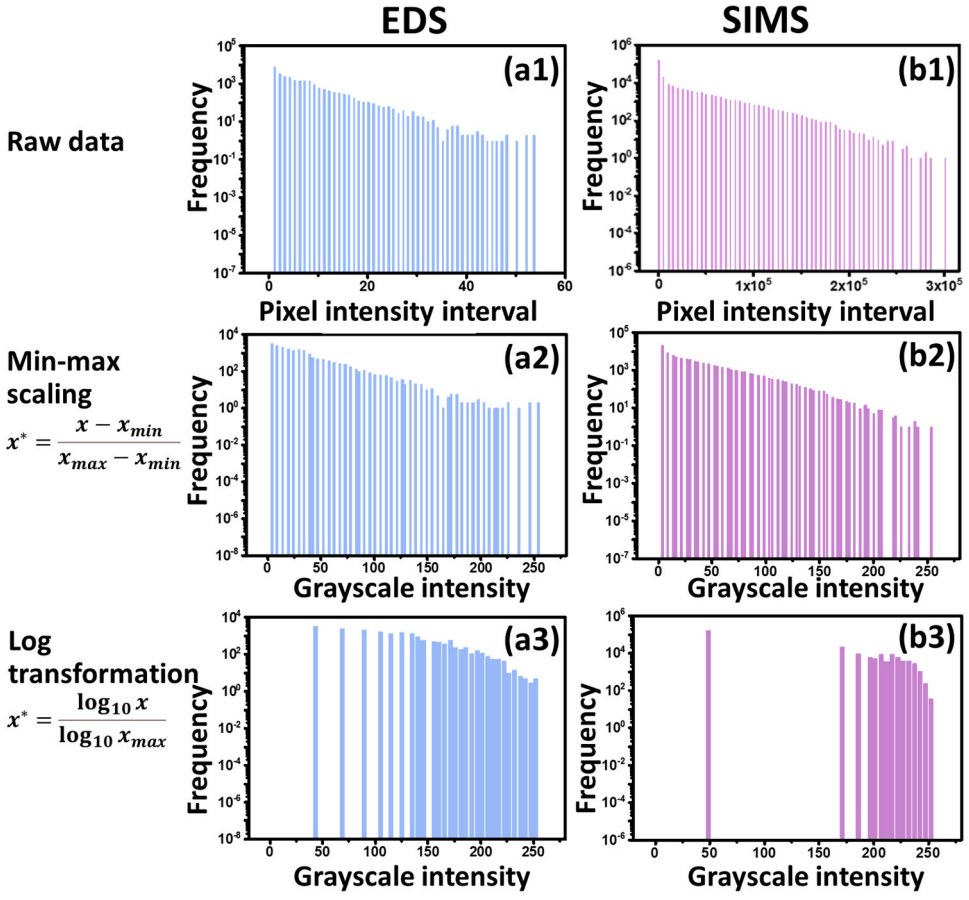

Fig. 2. Typical EDS and SIMS mapping data. Intensity frequency distribution for raw (a1) EDS and (b1) SIMS datasets; Grayscale histograms for (a2) EDS and (b2) SIMS datasets normalized by min-max scaling Eqs. (1), and (a3) EDS and (b3) SIMS datasets normalized by a log transformation Eq. (2).

value, X_{max} is the highest intensity and x_{min} is the lowest intensity.

Figs. 2(b) and 2(c) show the intensity frequency distribution for the SIMS and EDS data for the two normalization approaches. Both min-max scaling and log transformation normalizations distributed the pixel intensity to the same grayscale [0, 255]. The min-max scaling produced counts across the grayscale whereas the logarithmic approach clustered the data to higher grayscale, especially in the case of the SIMS data.

Fig. 3(a) depicts a standard EDS raw intensity data map before any normalization, while Figs. 3(b) and 3(c) display the same images post-normalization using the min-max and logarithmic approaches, respectively. Zoomed-in views of the identical image region are presented in Figs. 3(d) to 3(f). Notably, the min-max approach exhibits sensitivity to outliers in the data, as evidenced in Fig. 3(g), which shows falsely removed pixels from the raw data during min-max normalization. In contrast, Fig. 3(h) shows there was no falsely removed pixel during the logarithm normalization, and the function of the logarithmic normalization was only to increase the dynamic range. As a result, for subsequent work, we applied the logarithmic normalization to both EDS and SIMS data sets. The normalized tif images (grayscale, 8-bit) were then imported to Avizo software package (Thermo Fisher Scientific Inc.) for further processing as described below.

The built-in Resample module based on the Lanczos filter implemented in Avizo was used to resample SIMS data sets into the same voxel size as the EDS data sets ($81.4 \times 81.4 \times 60\ nm^3$) *i.e.* the EDS data set was used as the reference grid. At the end of this process, EDS and SIMS data sets were expressed at the same data scale, grayscale, and voxel size.

2.4. 3D reconstruction and correlation between elemental mappings

The Transform Editor module in Avizo was used to align the datasets. Then, the Register Images module was applied to explore various correlations between the EDS and SIMS datasets. The Volume Rendering module was used to visualize the EDS and SIMS data sets in 3D. A built-in Correlation Histogram module was applied to investigate any spatial correlation between elements in the two data sets. The correlation coefficient of the voxel pairs was calculated via Sample Covariance:

$$Cov(A,B) = \frac{\sum (A_i - \mu) \times (B_i - \mu)}{n - 1} \quad (3)$$

where Cov(A,B) is the covariance of data set A and covariance of data set B. $\sum (A_i) = \mu$ is the expected mean value for A, and $\sum (B_j) = v$ is the expected mean value for B. $\sum$is the summation operation of the data points from each sample, and n is the number of data points in the sample set.

3. Results and discussion

Fig. 4 shows a BSE image (Fig. 4(a)) of the electrode cross-section, corresponding EDS elemental maps (Fig. 4(b)) and SIMS map (Fig. 4(d)). The EDS maps were used to identify the 4 constituent materials: LLZTO, LCO, Al_2O_3 and SP, identified using Zr Lα1, Co Lα1,2, Al Kα1, and C Kα1_2 EDS maps respectively. A SIMS map was utilized to map the distribution of Li. Backscattered electron yield from the heavier elements (Pt Z = 78, Zr Z = 40) was stronger than from light elements (Co Z = 27, Al Z = 13, and C Z = 6), and so materials rich in heavy elements appeared brighter. Examples of each material are labeled in Fig. 4(c), which is a zoomed-in region of Fig. 4(a). LLZTO particles had diameters ranging from 2 to 8 μm while LCO particles were smaller, spanning the range sub-micron to 3 μm. The carbon SP could only be resolved where present as agglomerates of a few μm or larger. The mixing of the different particulates was somewhat inhomogeneous and typical of this type of electrode, but suggested sufficient carbon and LLZTO interconnection to facilitate electron and ion percolation, respectively. The electrode cross-section was relatively dense (the black regions are SP agglomerates rather than pores) although there was some particle cracking that was due to the high pressures used in electrode fabrication.

Fig. 5(a) shows a BSE image of a smaller region of the same electrode,

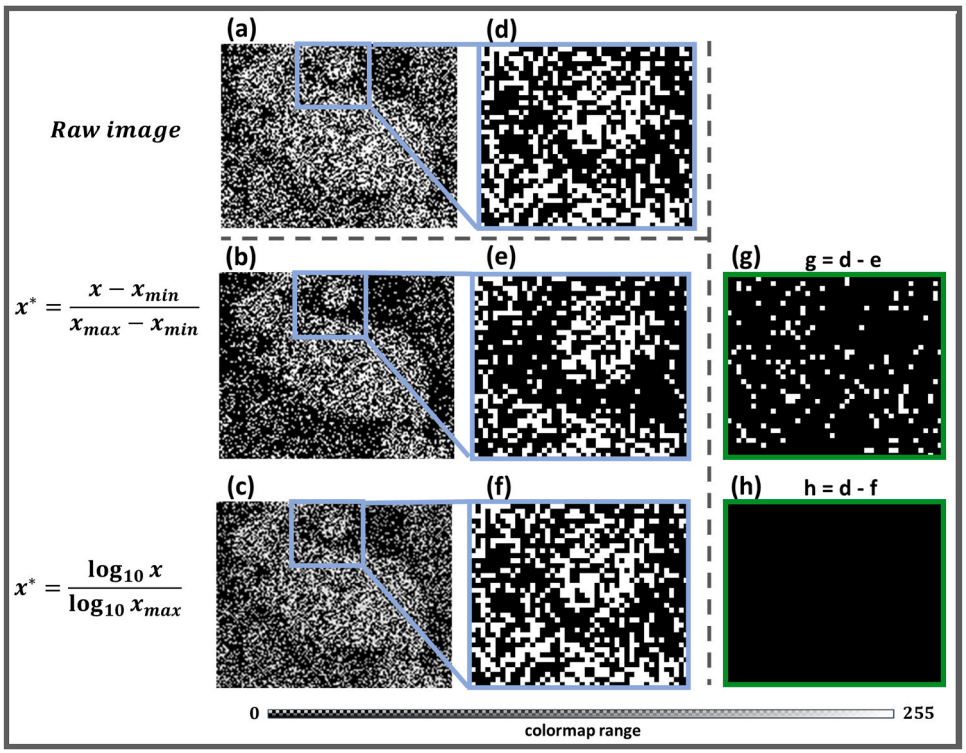

Fig. 3. Grayscale images of the typical Zr distribution in an LLZTO/Al_2O_3-coated-LCO/SP electrode obtained by EDS: (a) raw image, mapping normalized via (b) min-max scaling Eq. (1) and (c) log transformation Eq. (2). (d), (e), (f) Zoomed-in views of (a), (b), and (c) respectively. (g) The difference between (d) and (e), (h) the difference between (d) and (f).

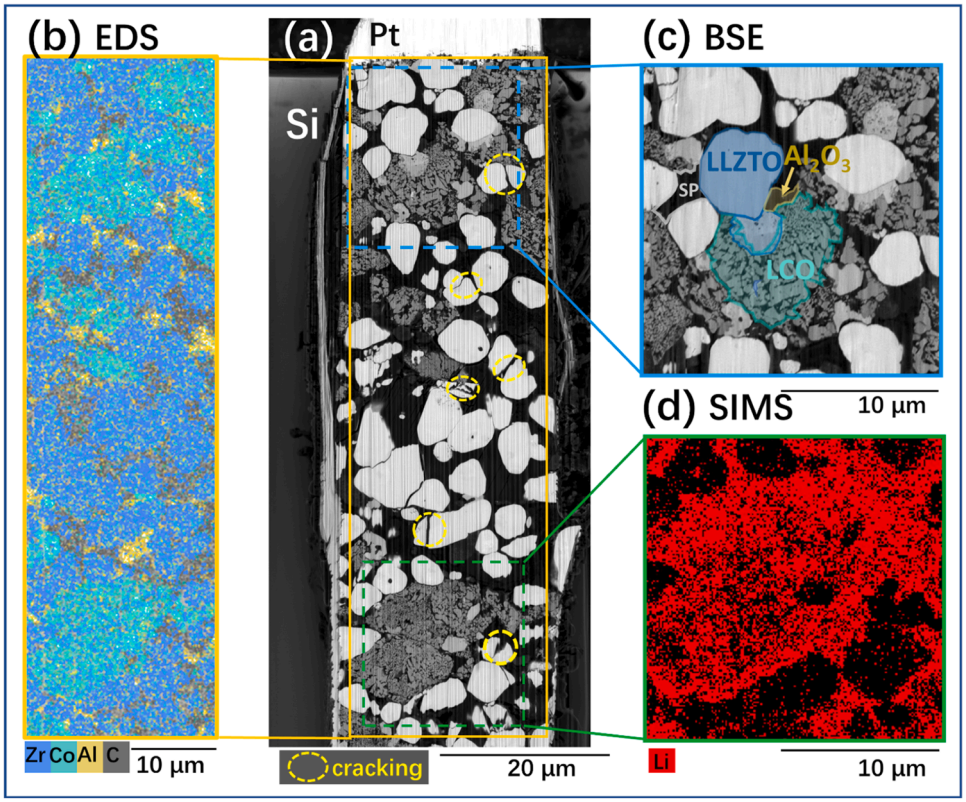

Fig. 4. An electrode cross-section. (a) BSE image with cracking marked by blue circles. (b) EDS maps of Zr Lα1, Co Lα1,2, Al Kα1, and C Kα1_2. (c) Zoomed-in view of the BSE image of the upper section of (a). (d) Zoomed-in view of the SIMS Li map of the lower section of (a).

which was investigated by multilayer removal using the Xe^+ plasma, and a series of EDS and SIMS based maps. The total depth of removed material was 2.3 μm in 39 layers, giving a total removed volume of 605 μm^3. Fig. 5(b) shows a 3D Li count map on the same scale, and covering a relatively large area (and volume), compared with previous work using FIB-based techniques, although conventional FIB approaches are steadily increasing removal areas/volumes (Sun et al., 2020; Li et al., 2017; Xu et al., 2017). Figs. 5(c) to 5(g) show the 3D reconstruction of all elemental maps, combining EDS and SIMS data. Li was detected in almost all volumes with the higher intensity in the LCO particles. Some of LCO particles had apparently varying Li intensity within a single particle. As previously mentioned, care must be taken in correlating detected species intensity with concentration, since the SIMS yield of species under the ion beam depends on factors in addition to local element concentration. The BSE image in Fig. 5(a) shows the LCO particles had a more complex internal microstructure than the LLZO particles that were largely featureless. Movie S1 in the Supporting Information presents a 3D animation of the volume reconstruction. Each voxel had dimensions 81.4 × 81.4 × 60 nm^3.

Supplementary material related to this article can be found online at doi:10.1016/j.micron.2024.103746.

Figs. 6(a) and 6(b) display 2D maps of Li and Zr, respectively taken from the same dataset as Fig. 5. Both are 8-bit images using the same color scale where a high pixel intensity, approaching 255, is shown red, and low intensity shown in blue. In general, the Li-rich and Zr-rich areas were separate. Fig. 6(c) plots Cov(A, B) from Eq. (3) where A = Li in Fig. 6(a) and B = Zr in Fig. 6(b). Each pixel in Fig. 6(c) has the product of Cov(A, B), normalized between 0 and 255, so high values corresponded to high Li × Zr intensity. The approximately central particle in the image, and the surrounding smaller particles, had relatively high Li × Zr intensity and was therefore identified as LLZTO; the majority of the other particles in the image were LCO. Fig. 6(c) shows that within the larger LLZTO particle, the local Li × Zr product showed regions of relatively high intensity, high- lighted by the accompanying line scan that plots the intensity across the particle. The edges of the particle were a region of relatively high intensity and were ascribed to the comparative enrichment of Zr due to a comparative loss of Li from the particle surface due to exposure to high temperature during processing (Huang et al., 2017). Several other LLZTO particles showed similar internal features. Although a relatively small volume was studied here at high resolution to establish the workflow, it can be applied to fields of view up to 700 μm × 700 μm.

There are several potential sources of error, both in data acquisition and post-processing. For spatial measurements (x, y), calibrating the microscope to a known standard reduced location error to approximately 0.1 μm over 100 μm (about 0.1 %). For chemical analyses, the X-ray maps were normalized and qualitative, indicating only the relative distribution of elements within one image. SIMS analysis is similarly qualitative and quantification only possible using reference standards of known, appropriate composition, *i.e.* close to the specimen composition and the determination of relative sensitivity factors (RSFs) for each element (Christien et al., 2012). SIMS quantification is particularly sensitive for Li, due to its high sputter yield, low mass, and high probability of ionization (Laufer et al., 2011; Wilson 1995). Indeed, Li is among the most sensitive elements in SIMS and can be detected in both negative and positive ion modes. Depending on the primary ion source, instrument, and the presence of any matrix effects, Li can be detected at levels as low as ppb (Williams 1985; Odom 1994). However, in this case, we are not focusing on trace amounts of Li and focus only on spatial variations of relative concentration.

Based on this proof of concept study, several improvements for co-milling/ EDS/SIMS can be suggested. (i) Automation of the 'rocking' between positions for layer removal/milling, EDS measurement, and SIMS measurement. (ii) Addition of a cryo-stage, since although the Xe-ion plasma beam induces less damage compared with a Ga-ion beam (Burnett et al., 2016), Li mobility might be expected within the sample

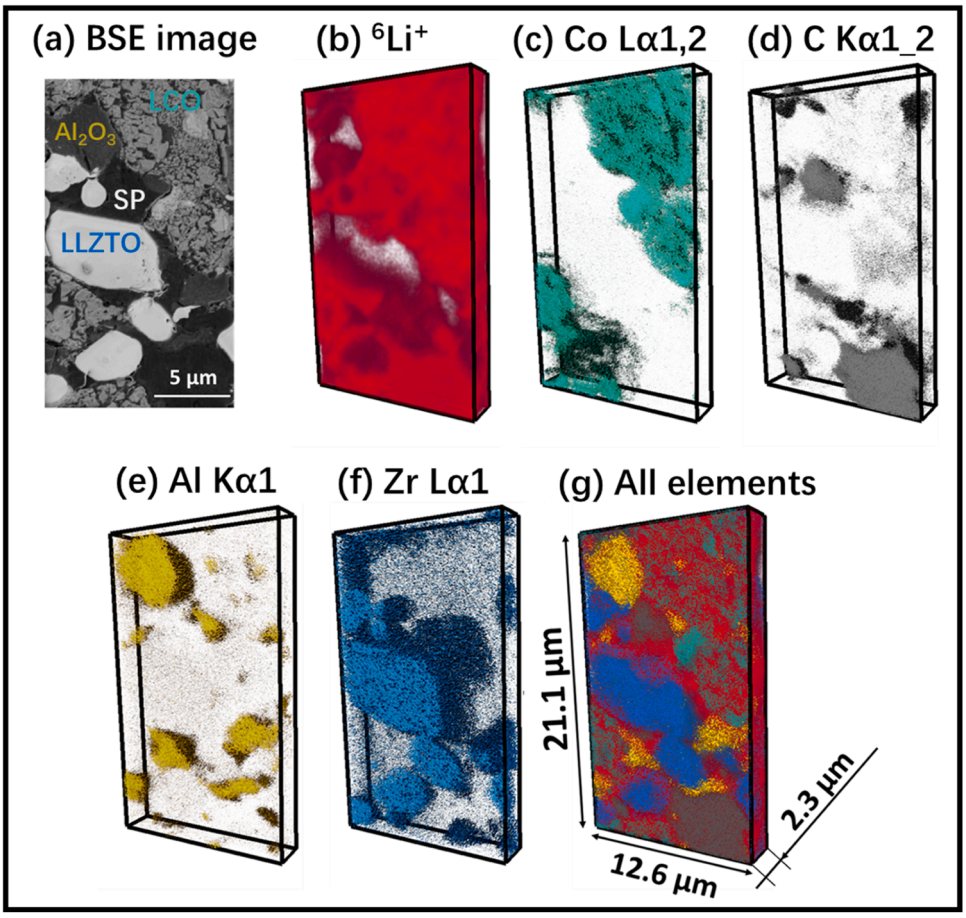

Fig. 5. 3D reconstruction of an LLZTO/Al_2O_3-coated-LCO/SP electrode elemental maps. (a) BSE image of the electrode cross-section before milling/layer removal. Elemental maps of (b) ^{6}Li+ obtained by SIMS and (c) Co Lα1,2, (d) C Kα1_2, (e) Al Kα1, (f) Zr Lα1 obtained by EDS, (g) 3D reconstruction of combined SIMS and EDS maps (b) to (f).

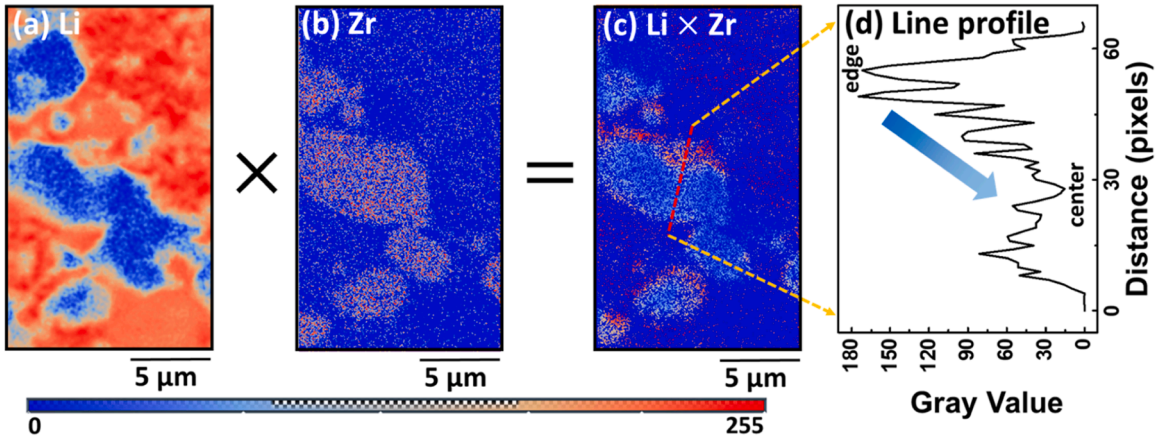

Fig. 6. (a) Li map obtained by SIMS. (b) Zr map obtained by EDS. (c) Li × Zr map based on Eq. (3). (d) Line profile of Li × Zr.

under beam excitation, which will be reduced by the use of a cryo-stage. (iii) Conditions for X-ray mapping can be further optimised by reducing the accelerating voltage of the SEM and selecting the L or M lines of the desired element, which would reduce the interaction volume, and improve the spatial resolution of the maps. (iv) The Xe-ion milling might be combined with laser milling to increase the speed and depth of sections. (Gholinia et al., 2024; Winiarski and Geurts 2020) (v) SIMS detection sensitivity varies by element, and for example, we observed that while there was a high yield and sensitivity for Li (and our SIMS was optimized for Li resolution), the sputter rate and/or detection sensitivity for Zr and Ta were much less favorable. This highlights the importance of understanding yield effects in SIMS, and performing calibration or comparative analyses with other techniques where possible, such as EDS maps of Zr and Ta distributions as performed here. (vi) Methods to calibrate the Li-based SIMS intensity counts with local Li elemental concentration might be developed.

4. Conclusions

We have combined SIMS-based maps of Li-containing species with EDS-based maps of other elements obtained in 3D in a Xe-ion based plasma-FIB instrument, and applied the new methodology to a LLZTO/Al_20_3-coated-LCO/ SP composite cathode for a solid-state battery. Because SIMS and EDS data were obtained from slightly different 2D regions and at different resolutions, off-line tools were developed that allowed the accurate reconciliation of the different data types in 3D. Although the Xe-ion P-FIB platform in principle offers a wide range of resolutions that could be explored, in this proof-of-concept, the spatial resolution of the reconstructed voxels each containing EDS and SIMS data was 81.4 × 81.4 × 60 nm^3. Local correlations between normalised Li (from SIMS) and Zr (from EDS) intensity data were demonstrated in 2D, and would be readily extensible to 3D. A number of improvements were suggested such as greater automation of the stage motion between milling and mapping orientations, a cryo-stage to suppress movement of mobile species such as Li under beam excitation, and strategies to improve the quantitative capability of the SIMS data.

CRediT authorship contribution statement

Yige Sun: Writing – original draft, Visualization, Validation, Software, Methodology, Investigation, Formal analysis, Conceptualization. **Gareth M. Hughes:** Writing – review & editing, Resources, Methodology, Conceptualization. **Junliang Liu:** Writing – review & editing. **Junfu Bu:** Writing – review & editing, Resources. **Patrick S. Grant:** Writing – review & editing, Supervision, Methodology, Funding acquisition, Conceptualization. **Chris R.M. Grovenor:** Writing – review & editing, Methodology.

Declaration of Competing Interest

The authors declare that they have no known competing financial interests or personal relationships that could have appeared to influence the work reported in this paper.

Acknowledgments

We would like to thank the Faraday Institution for financial support via projects Nextrode (FIRG015/FIRG066) and SOLBAT (FIRG026). The authors acknowledge the use of characterisation facilities within the David Cockayne Centre for Electron Microscopy at the Department of Materials, University of Oxford, alongside financial support provided by EPSRC "University of Oxford: experimental equipment upgrade" (EP/M02833X/1) and the Henry Royce Institute (Grant EP/R010145/1). YS thanks Linacre College, University of Oxford for a David Cockayne Fellowship, and Dr. Andreas Staude from Thermo—Fisher and Zuse Institute Berlin for valuable discussion.

Appendix A. Supporting information

Supplementary data associated with this article can be found in the online version at doi:10.1016/j.micron.2024.103746.

Data availability

The data that support the findings of this study are available from the corresponding authors upon reasonable request.

References

Brown, A., Berg, J.A.Van den, Vickerman, J.C., 1986. The application of secondary ion mass spectrometry to surface analysis of semiconductor substrates and devices. Surf. Interface Anal. 9 (5), 309–317.

Brugge, Rowena H., Chater, Richard J., Kilner, John A., Aguadero, Ainara, 2021. Experimental determination of Li diffusivity in LLZO using isotopic exchange and FIB-SIMS. J. Phys.: Energy 3 (3), 034001.

Bu, Junfu, Jönsson, P.är G.öran, Zhao, Zhe, 2016. Transport properties of $BaZr_{0\text{-}5}Ce_{0.3}Y_{0.2}0_{3\text{-}\delta}$ proton conductor prepared by spark plasma sintering. Ceram. Int. 42 (3), 4393–4399.

Bucci, Giovanna, Swamy, Tushar, Chiang, Yet-Ming, Carter, W.Craig, 2017. Modeling of internal mechanical failure of all-solid-state batteries during electrochemical cycling, and implications for battery design. J. Mater. Chem. A 5 (36), 19422–19430.

Burnett, T.L., Kelley, Ron, Winiarski, Bart, Contreras, L., Daly, Michael, Gholinia, Ali, Burke, M.G., Withers, P.J., 2016. Large volume serial section tomography by Xe Plasma FIB dual beam microscopy. Ultramicroscopy 161, 119–129.

Cantoni, Marco, Holzer, Lorenz, 2014. Advances in 3D focused ion beam tomography. Mrs Bull. 39 (4), 354–360.

Christien, Frederic, Downing, C., Moore, K.L., Grovenor, C.R.M., 2012. Quantification of grain boundary equilibrium segregation by NanoSIMS analysis of bulk samples. Surf. Interface Anal. 44 (3), 377–387.

Doerrer, Christopher, Capone, Isaac, Narayanan, Sudarshan, Liu, Junliang, Grovenor, Chris R.M., Pasta, Mauro, Grant, Patrick S., 2021. High energy density single-crystal NMC/Li_6PS_5Cl cathodes for all-solid-state lithium-metal batteries. ACS Appl. Mater. Interfaces 13 (31), 37809–37815.

Dominic Spencer-Jolly, Agarwal, Varnika, Doerrer, Christopher, Hu, Bingkun, Zhang, Shengming, Melvin, Dominic L.R., Gao, Hui, Gao, Xiangwen, Adamson, Paul, Magdysyuk, Oxana V., et al., 2023. Structural changes in the silver-carbon composite anode interlayer of solid-state batteries. In: Joule, 7, pp. 503–514.

Fang, Yuan, Smith, Alexander J., Lindstrom, Rakel Wreland, Lindbergh, Goran, Fur, Istvan, 2022. Quantifying lithium lost to plating and formation of the solid-electrolyte interphase in graphite and commercial battery components. Appl. Mater. Today 28, 101527.

Gholinia, A., Donoghue, J., Garner, A., Curd, M., Lawson, M.J., Winiarski, B., Geurts, R., Withers, P.J., Burnett, T.L., 2024. Exploration of fs-laser ablation parameter space for 2D/3D imaging of soft and hard materials by tri-beam microscopy. Ultramicroscopy 257, 113903.

Gong, Yue, Chen, Yuyang, Zhang, Qinghua, Meng, Fanqi, Shi, Jin-An, Liu, Xinyu, Liu, Xiaozhi, Zhang, Jienan, Wang, Hao, Wang, Jiangyong, et al., 2018. Three-dimensional atomic-scale observation of structural evolution of cathode material in a working all-solid-state battery. Nat. Commun. 9 (1), 3341.

Guilhaus, M., 2005. Mass spectrometry — time-of-flight. In: Worsfold, Paul, Townshend, Alan, Poole, Colin (Eds.), Encyclopedia of Analytical Science (Second Edition), second ed. Elsevier, Oxford, pp. 412–423.

Gurung, Ashim, Pokharel, Jyotshna, Baniya, Abiral, Pathak, Rajesh, Chen, Ke, Lamsal, Buddhi Sagar, Ghimire, Nabin, Zhang, Wen-Hua, Zhou, Yue, Qiao, Qiquan, 2019. A review on strategies addressing interface incompatibilities in inorganic all-solid-state lithium batteries. Sustain. Energy Fuels 3 (12), 3279–3309.

Hovington, Pierre, Timoshevskii, Vladimir, Burgess, Simon, Demers, Hendrix, Statham, Peter, Gauvin, Raynald, Zaghib, Karim, 2016. Can we detect Li K X-ray in lithium compounds using energy dispersive spectroscopy? Scanning 38 (6), 571–578.

Huang, Zeya, Liu, Kai, Chen, Linhui, Lu, Yirui, Li, Yutao, Wang, Chang-An, 2017. Sintering behavior of garnet-type $Li_{6.4}La_3Zr_{1.4}Ta_{0.6}0_{12}$ in Li_2CO_3 atmosphere and its electrochemical property. Int. J. Appl. Ceram. Technol. 14 (5), 921–927.

Kim, Kun Joong, Rupp, Jennifer L.M., 2020. All ceramic cathode composite design and manufacturing towards low interfacial resistance for garnet-based solid-state lithium batteries. Energy Environ. Sci. 13 (2), 4930–4945.

Kim, Se-Ho, Antonov, Stoichko, Zhou, Xuyang, Stephenson, Leigh T., Jung, Chan-won, EI-Zoka, Ayman A., Schreiber, Daniel K., Conroy, Michele, Gault, Baptiste, 2022. Atom probe analysis of electrode materials for Li-ion batteries: challenges and ways forward. J. Mater. Chem. A 10 (9), 4926–4935.

Ko, Dong-Su, Park, Young Min, Kim, Sung-Dae, Kim, Young-Woon, 2007. Effective removal of Ga residue from focused ion beam using a plasma cleaner. Ultramicroscopy 107 (4-5), 368–373.

Koh, Hyeongjun, Detsi, Eric, Stach, Eric A., 2023. Understanding ion-beam damage to air-sensitive lithium metal with cryogenic electron and ion microscopy. Microsc. Microanal. 29 (4), 1350–1356.

Kuwata, Naoaki, Nakane, Masakatsu, Miyazaki, Takamichi, Mit-suishi, Kazutaka, Kawamura, Junichi, 2018. Lithium diffusion coefficient in $LiMn_2O_4$ thin films measured by secondary ion mass spectrometry with ion-exchange method. Solid State Ion. 320, 266–271.

Laegreid, Nils, Wehner, G.K., 1961. Sputtering yields of metals for Ar^+ and Ne^+ ions with energies from 50 to 600 eV. J. Appl. Phys. 32 (3), 365–369.

Laufer, Andreas, Volbers, Niklas, Eisermann, Sebastian, Potzger, Kay, Geburt, Sebastian, Ronning, Carsten, Meyer, Bruno K., 2011. Determination of secondary ion mass spectrometry relative sensitivity factors for polar and non-polar ZnO. J. Appl. Phys. 110 (9).

Li, Wangda, Kim, Un-Hyuck, Dolocan, Andrei, Sun, Yang-Kook, Manthiram, Aru-mugam, 2017. Formation and inhibition of metallic lithium microstructures in lithium batteries driven by chemical crossover. ACS Nano 11 (6), 5853–5863.

Lindon, John C., Tranter, George E., Koppenaal, David, 2016. Encyclopedia of spectroscopy and spectrometry. Academic Press.

Liu, Jinqiao, Niu, Ranming, Gu, Ji, Cabral, Matthew, Song, Min, Liao, Xiaozhou, 2020. Effect of ion irradiation introduced by focused ion-beam milling on the mechanical behaviour of sub-micron-sized samples. Sci. Rep. 10 (1), 1–8.

Manawan, Maykel, Kartini, Evvy, Avdeev, Maxim, 2021. Visualizing lithium ions in the crystal structure of Li_3PO_4 by in situ neutron diffraction. J. Appl. Crystallogr. 54 (5), 1409–1415.

Marker, Katharina, Xu, Chao, Grey, Clare P., 2020. Operando NMR of NMC811/graphite lithium-ion batteries: structure, dynamics, and lithium metal deposition. J. Am. Chem. Soc. 142 (41), 17447–17456.
Mei, Hao, Laws, Travis S., Terlier, Tanguy, Verduzco, Rafael, Stein, Gila E., 2022. Characterization of polymeric surfaces and interfaces using time-of-flight secondary ion mass spectrometry. J. Polym. Sci. 60 (7), 1174–1198.
Metcalf, Leigh, Casey, William, 2016. Introduction to data analysis. Cyber -Curity Appl. Math. 43–65.
Moore, Katie L., Schroder, Markus, Grovenor, Chris R.M., 2012. Imaging secondary ion mass spectroscopy. Handb. Nanoscopy 709–744.
Ning, Ziyang, Li, Guanchen, Melvin, Dominic L.R., Chen, Yang, Bu, Junfu, Spencer-Jolly, Dominic, Liu, Junliang, Hu, Bingkun, Gao, Xiangwen, Perera, Johann, et al., 2023. Dendrite initiation and propagation in lithium metal solid-state batteries. Nature 618 (7964), 287–293.
Nomura, Yuki, Yamamoto, Kazuo, Hirayama, Tsukasa, Ohkawa, Mayumi, Igaki, Emiko, Hojo, Nobuhiko, Saitoh, Koh, 2018. Quantitative operando visualization of electrochemical reactions and li ions in all-solid-state batteries by STEM-EELS with hyperspectral image analyses. Nano Lett. 18 (9), 5892–5898.
Nomura, Yuki, Yamamoto, Kazuo, Fujii, Mikiya, Hirayama, Tsukasa, Igaki, Emiko, Saitoh, Koh, 2020b. Dynamic imaging of lithium in solid-state batteries by operando electron energy-loss spectroscopy with sparse coding. Nat. Commun. 11 (1), 2824.
Nomura, Yuki, Yamamoto, Kazuo, Hirayama, Tsukasa, Igaki, Emiko, Saitoh, Koh, 2020a. Visualization of lithium transfer resistance in secondary particle cathodes of bulk-type solid-state batteries. ACS Energy Lett. 5 (6), 2098–2105.
Odom, Robert W., 1994. Second. Ion.-. Mass Spectrom. Imaging *Appl. Spectrosc. Rev.* 29 (1), 67–116.
Ohnishi, Miwa, Matsuoka, Osamu, Nogi, Hidenobu, Sakamoto, Tetsuo, 2012. Observation of a $LiCoO_2$ cathode material of a li-ion battery by high spatial resolution TOF-SIMS. e-J. Surf. Sci. Nanotechnol. 10, 207–209.
Osterreicher, Johannes A., Simson, Clemens, GroBalber, Alexander, Frank, Simon, Gneiger, Stefan, 2021. Spatial lithium quantification by backscattered electron microscopy coupled with energy-dispersive X-ray spectroscopy. Scr. Mater. 194, 113664.
Otoyama, Misae, Ito, Yusuke, Hayashi, Akitoshi, Tatsumisago, Masahiro, 2016. Raman imaging for $LiCoO_2$ composite positive electrodes in all-solid-state lithium batteries using Li_2S-P_2S_5 solid electrolytes. J. Power Sources 302, 419–425.
Pasta, Mauro, Armstrong, David, Brown, Zachary L., Bu, Junfu, Castel!, Martin R., Chen, Peiyu, Cocks, Alan, Corr, Serena A., Cussen, Edmund J., 2020. 2020 roadmap on solid-state batteries (Ed Darnbrough, et al). In: Journal of Physics: Energy, 2, 032008 (Ed Darnbrough, et al).
Pattammattel, Ajith, Tappero, Ryan, Ge, Mingyuan, Chu, Yong S., Huang, Xiaojing, Gao, Yuan, Yan, Hanfei, 2020. High-sensitivity nanoscale chemical imaging with hard x-ray nano-XANES. Sci. Adv. 6 (37), eabb3615.
Pillatsch, Lex, Ostlund, Fredrik, Michler, Johann, 2019. FIBSIMS: A review of secondary ion mass spectrometry for analytical dual beam focussed ion beam instruments. Prog. Cryst. Growth Charact. Mater. 65 (1), 1–19.
Randau, Simon, Weber, Dominik A., Kötz, Olaf, Koerver, Raimund, Braun, Philipp, Weber, André, Ivers-Tiffée, Ellen, Adermann, Torben, Kulisch, J.örn, Zeier, Wolfgang G., et al., 2020. Benchmarking the performance of all-solid-state lithium batteries. *Nat. Energy* 5 (3), 259–270.
Ren, Yaoyu, Danner, Timo, Moy, Alexandra, Finsterbusch, Martin, Hamann, Tanner, Dippell, Jan, Fuchs, Till, Muller, Marius, Hoft, Ricky, Weber, Andre, et al., 2023. Oxide-based solid-state batteries: a perspective on composite cathode architecture. Adv. Energy Mater. 13 (1), 2201939.
Robertson, Stuart, Doak, Scott, Sun, Fu-Long, Liu, Zhi-Quan, Liu, Changqing, Zhou, Zhaoxia, 2020. Focused ion beam preparation of microbeams for in situ mechanical analysis of electroplated nanotwinned copper with probe type indenters. J. Microsc. 279 (3), 212–216.
Robinson, James B., Maier, Maximilian, Alster, George, Compton, Tomos, Brett, Dan J.L., Shearing, Paul R., 2019. Spatially resolved ultrasound diagnostics of li-ion battery electrodes. Phys. Chem. Chem. Phys. 21 (12), 6354–6361.
Schaffer, Miroslava, Wagner, Julian, Schaffer, Bernhard, Schmied, Mario, Mulders, Hans, 2007. Automated three-dimensional X-ray analysis using a dual-beam FIB. Ultramicroscopy 107 (8), 587–597.
Stevie, F.A., Sedlacek, L., Babor, P., Jiruse, J., Principe, E., Klosova, K., 2014. FIB-SIMS quantification using TOF-SIMS with Ar and Xe plasma sources. Surf. Interface Anal. 46 (S1), 285–287.
Sun, H.Hohyun, Dolocan, Andrei, Weeks, Jason A., Heller, Adam, Mullins, C.Buddie, 2020. Stabilization of a highly Ni-rich layered oxide cathode through flower-petal grain arrays. ACS Nano 14 (12), 17142–17150.
Torres, Allan M., Price, William S., 2016. Common problems and artifacts encountered in solution-state NMR experiments. Concepts Magn. Reson. Part A 45 (2), e21387.
Trease, Nicole M., Zhou, Lina, Chang, Hee Jung, Zhu, Ben Yunxu, Grey, Clare P., 2012. In situ NMR of lithium ion batteries: Bulk susceptibility effects and practical considerations. Solid State Nucl. Magn. Reson. 42, 62–70.
Treat, Neil D., Brady, Michael A., Smith, Gordon, Toney, Michael F., Kramer, Edward J., Hawker, Craig J., Chabinyc, Michael L., 2011. Interdiffusion of PCBM and P3HT reveals miscibility in a photovoltaically active blend. Adv. Energy Mater. 1 (1), 82–89.
Werner, H.W., 1980. Quantitative secondary ion mass spectrometry: A review. Surf. Interface Anal. 2 (2), 56–74.
Whitlow, Harry J., Hautala, Mikko, Sundqvist, Bo.U.R., 1987. Collision cascade parameters for slow particles impinging on biomolecule targets. Int. J. Mass Spectrom. Ion.-. Process. 78, 329–340.
Wilhelm, Gudrun, Golla-Schindler, Ute, War!, Katharina, Geis-bauer, Christian, Cooke, Graham, Bernthaler, Timo, Schweiger, Hans-Georg, Schneider, Gerhard, 2024. Influence of water on aging phenomena of calendric stored and cycled Li-ion batteries. Nanoenergy Adv. 4 (2), 174–195.
Williams, Peter, 1985. Secondary ion mass spectrometry. Annu. Rev. Mater. Sci. 15 (1), 517–548.
Wilson, R.G., 1995. SIMS quantification in Si, GaAs, and diamond-an update. Int. J. Mass Spectrom. Ion.-. Process. 143, 43–49.
Winiarski, Bartiomiej, Geurts, Remco, 2020. Laser Xe^+ Plasma FIB-SEM: Correlative microscopy of 3D microstructures from nanometers to millimeters. *Microscopy and Analysis*. EMEA *S3–58*.
Wood, Kevin N., Steirer, K.Xerxes, Hafner, Simon E., Ban, Chunmei, Santhanagopalan, Shriram, Lee, Se-Hee, Teeter, Glenn, 2018. Operando X-ray photoelectron spectroscopy of solid electrolyte interphase formation and evolution in Li_2S-P_2S_5 solid-state electrolytes. Nat. Commun. 9 (1), 2490.
Xu, C.Shan, Hayworth, Kenneth J., Lu, Zhiyuan, Grob, Patricia, Hassan, Ahmed M., Garcia-Cerdan, Jose G., Niyogi, Krishna K., Nogales, Eva, Weinberg, Richard J., Hess, Harald F., 2017. Enhanced FIB-SEM systems for large-volume 3D imaging. elife 6, e25916.
Yamagishi, Yuji, Morita, Hiromi, Nomura, Yuki, Igaki, Emiko, 2020. Visualizing lithium distribution and degradation of composite electrodes in sulfide-based all-solid-state batteries using operando time-of-flight secondary ion mass spectrometry. ACS Appl. Mater. Interfaces 13 (1), 580–586.
Yim, Chae-Ho, Houache, Mohamed S.E., Baranova, Elena A., Abu-Lebdeh, Yaser, 2023. Understanding key limiting factors for the development of all-solid-state-batteries. Chem. Eng. J. Adv. 13, 100436.
Ziesche, Ralf F., Tremsin, Anton S., Huang, Chun, Tan, Chun, Grant, Patrick S., Storm, Malte, Brett, Dan J.L., Shearing, Paul R., Kockelmann, Winfried, 2020. 4D Bragg edge tomography of directional ice templated graphite electrodes. J. Imaging 6 (12), 136.